



## Double grating shearing interferometry for X-ray free-electron laser beams

MIKAKO MAKITA,<sup>1,4</sup> GEDIMINAS SENIUTINAS,<sup>2</sup> MATTHEW H. SEABERG,<sup>3</sup> HAE JA LEE,<sup>3</sup> ERIC C. GALTIER,<sup>3</sup> MENGNING LIANG,<sup>3</sup> ANDREW AQUILA,<sup>3</sup> SÉBASTIEN BOUTET,<sup>3</sup> AKEL HASHIM,<sup>3</sup> MARK S. HUNTER,<sup>3</sup> TIM VAN DRIEL,<sup>3</sup> ULF ZASTRAU,<sup>1</sup> CHRISTIAN DAVID,<sup>2</sup> AND BOB NAGLER<sup>3,5</sup>

<sup>1</sup>European XFEL, Holzkoppel 4, 22869 Schenefeld, Germany

<sup>2</sup>Paul Scherrer Institut, Forschungsstrasse 111, 5232 Villigen PSI, Switzerland

<sup>3</sup>SLAC National Accelerator Laboratory, 2575 Sand Hill Road, Menlo Park, California 94025, USA

<sup>4</sup>e-mail: mikako.makita@xfel.eu

<sup>5</sup>e-mail: bnagler@slac.stanford.edu

Received 14 February 2020; revised 18 March 2020; accepted 20 March 2020 (Doc. ID 390601); published 28 April 2020

The advancements in bright and coherent X-ray free-electron lasers (XFEL) have in the last decade revolutionized diverse fields of study, leading to an ever-increasing demand in more intense X-ray pulses. The accurate knowledge of the wavefront and the focal profile of such pulses ultimately dictates much of the experimental outcome. Here we present a single-shot shearing interferometry method to measure the wavefront of a focused hard XFEL pulse. Two identical transmission gratings are placed near the focus, and the interference pattern of overlapping diffraction orders is analyzed, resulting in a two-dimensional reconstruction of the X-ray wavefront. The spatial resolution and wavefront sensitivity can be tuned *in-situ* during the measurement. The method is non-invasive (i.e., the zeroth order or transmitted pulse is not modified in intensity or profile), allowing for either a simultaneous intensity measurement at high resolution or a fully characterized transmitted pulse for general experimental use. © 2020 Optical Society of America under the terms of the OSA Open Access Publishing Agreement

<https://doi.org/10.1364/OPTICA.390601>

### 1. INTRODUCTION

The knowledge of focus parameters of X-ray free-electron lasers (XFEL) plays a pivotal role, not only for machine operators, but also in the fields that rely on the highest X-ray intensities and fluences. Relevant fields include anomalous nonlinear X-ray Compton scattering [1], the formation of hollow atoms [2], radiation damage studies on protein micro-crystals [3], and dense plasma science [4], to name a few. Therefore, a significant effort has gone into characterizing the wavefront and focal spot of X-ray pulses at FELs. Methods relying on imprints and ablations of material have been developed and are routinely used [5]. For hard X-rays, several methods were developed, such as scanning coherent diffraction microscopy or ptychography [6], Ronchi shearing interferometry [7,8], and Talbot interferometry [9–13].

In this report, we present a method called double grating shearing interferometry (DGSI), where two gratings are used to interfere with the first-order diffraction of each grating. The resulting fringes can be analyzed for full wavefront reconstruction of a single XFEL pulse. The reconstruction resolution and sensitivity depend on the grating positioning and orientation, and on the fringe period. These parameters can easily be tuned and optimized *in-situ*. We demonstrate this technique for nano-focused 8 keV X-rays at the coherent X-ray imaging endstation (CXI) [14,15] at Linac Coherent Light Source (LCLS).

### 2. EXPERIMENTAL CONCEPT

A schematic of the setup is shown in Fig. 1. The focus of the X-ray beam is defined as the origin of the  $z$ -axis. At  $z_1$ , a two-dimensional checkerboard phase grating is placed in the beam. A second identical grating is placed at a small distance  $\ell$  from the first grating. The spatial frequency of the gratings is such that the first diffraction orders are well separated from the transmitted pulse. The second diffraction grating is rotated around the optical axis by an angle  $\alpha$ . Due to this rotation, the incoming X-ray beam sees two distinct two-dimensional spatial frequencies (i.e., same magnitude but different direction), and the first diffraction orders from the two gratings are displaced with respect to each other on the X-ray camera, which we place at position  $z_2$  (see Fig. 1). The concept is similar to the one described in [16,17]. The interference fringe where the diffracted beams overlap can be analyzed in straightforward manner to reconstruct the wavefront profile of the X-ray beam. Similar to [7], we retrace the first-order diffracted beams of the grating back to their virtual foci. The two foci are displaced in both  $x$  and  $y$ , and they can be viewed as two point sources that will interfere in the far-field in the same way as the well-known Young's two-slit experiment. This analogy shows there is a linear phase between the two beams at the detector plane equal to

$$\Delta\phi = \frac{2\pi}{\lambda z_2} \tan\beta (s z_1 \alpha + n\ell) + \hat{S}_5(\phi_0(x, y)), \quad (1)$$

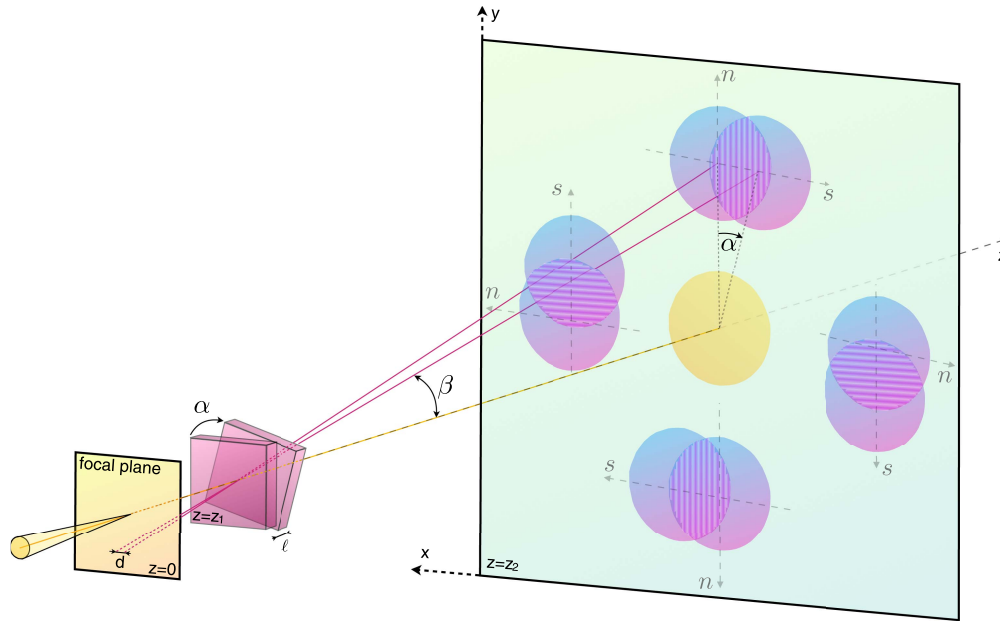


**Fig. 1.** Schematic of the setup. Two identical checkerboard gratings, separated by a distance  $\ell$ , are placed at distance  $z_1$  behind the focal plane of the X-rays. The second grating is rotated around the optical axis by a small angle  $\alpha$  with respect to the first grating (0.31 degrees in the data presented here). At a distance  $z_2$  behind the focal plane, an X-ray detector is placed, which captures the transmitted beam and the diffraction orders of the gratings (only the first-order diffractions of each grating are shown for clarity). Due to the rotation  $\alpha$  and the separation  $\ell$ , the first orders of different gratings are separated. Interference fringes, which contain the differential phase information of the beam, are seen where the first-order diffractions overlap (figure not to scale).

where  $s$  and  $n$  are the coordinates of a local axis system, as shown in Fig. 1:  $s$  is oriented along the shear direction due to the rotation of the second grating, and  $n$  is perpendicular to it.

In Eq. (1),  $\lambda$  is the wavelength of the X-rays,  $\beta$  is the first-order diffraction angle from the gratings,  $\alpha$  is the rotational angular difference between the two gratings, and  $\ell$  is the distance between the two gratings. The values of  $\alpha$  and  $\ell$  can be either measured or derived from the fringe frequency and orientation, or both.

Aberrations in the phase of the beam,  $\phi_0(x, y)$ , lead to distortions in the linear fringe pattern, as shown by the last term in Eq. (1). These distortions can be analyzed using standard Fourier transform methods [18] to yield the differential phase. It is important to note that the differential phase retrieved in this way is *not* the phase of the X-ray beam, but the phase difference of the two diffracted beams (i.e., the first orders of both gratings), as described by the shearing operator:

$$\hat{S}_s(\phi_0(x, y)) = \phi_0(x, y) - \phi_0(x - s_x, y - s_y), \quad (2)$$

with the shear values determined by the rotation of the second grating versus the first and the separation between both gratings. For example, for the top interference pattern in Fig. 1 this would lead to

$$s_x = \alpha(z_2 - z_1) \tan \beta, \quad (3)$$

$$s_y = \ell \tan \beta, \quad (4)$$

and similar equations can easily be derived for the other interferograms and shear directions. The method is a form of shearing interferometry, which is well described in the literature, and many methods exist to analyze the interferograms [19–23]. We opt to use a variation of the method previously employed in [7] and optimize the wavefront using two orthogonal differential phase

maps, originating from the top-right and bottom-right interferograms in Fig. 2. A more mathematically rigorous, albeit laborious and sleep-inducing, approach to justify Eqs. (1)–(3), and a full explanation of the optimization algorithm used, can be found in Supplement 1.

### 3. RESULTS

The experiment was carried out at the Coherent X-ray imaging endstation (CXI) [14,15] at LCLS. The LCLS X-ray beam of photon energy 8.5 keV is focused by a silicon-carbide-coated KB pair [24] with focal lengths of 900 mm in the horizontal and 500 mm in the vertical direction. Two transmission gratings were placed 35 mm behind the focus, with a separation of 0.68 mm between each other. An X-ray detector (Princeton Instrument PIXIS) was placed 1.72 m downstream the focus, which records both the transmitted beam and the diffraction orders of the gratings. Both gratings consist of identical checkerboard patterns, which are binary structures of a 96 nm pitch in both the  $x$ - and  $y$ -axis, etched into a diamond membrane and filled with Ir [25]. More details about the grating can be found in Supplement 1. The second grating was mounted on a rotation stage that allowed us to rotate the grating around the optical axis with respect to the first grating. In this way, the shearing fringe patterns were tuned *in-situ* by monitoring them directly on the detector. The optimum shearogram was judged based on the fringe frequency (about 10 pixels between the fringe pitch maxima to minima), and the intensity contrast of the fringes.

The recorded raw data on the X-ray camera can be seen in Fig. 2, where both the transmitted beam, as well as the first orders are clearly distinguished, and even other higher diffraction orders are visible. Due to the rectangular input aperture of the KB pair (the horizontal mirror has an aperture that is approximately 10% larger

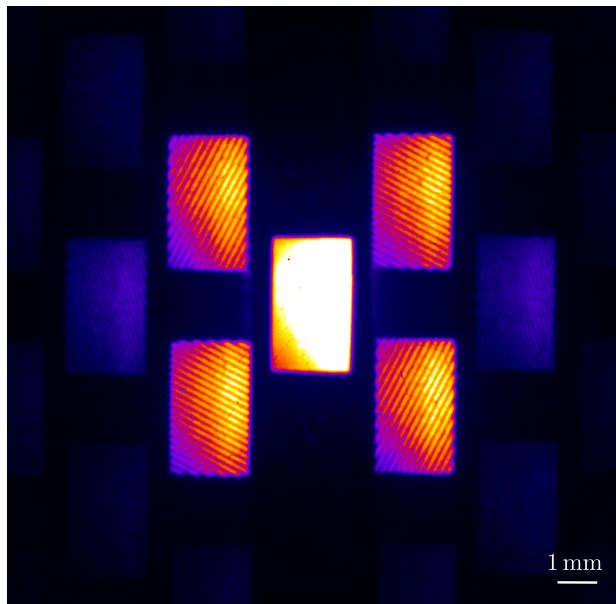


**Fig. 2.** Images of the X-ray beam on the camera. Due to the rectangular input aperture of the KB-focusing mirrors at CXI, and the rather large difference in the tangential and sagittal focal lengths, the beam shape at the camera position is rectangular. The orientation of the checkerboard was chosen to maximize the separation between the first orders and the transmitted pulse. The transmitted beam was attenuated with  $50\ \mu\text{m}$  of Cu taped on the camera scintillator to avoid saturation and keep the intensity levels comparable to those of the first orders.

than the vertical one), and the rather large difference in focal length of both mirrors, the beams on the detector have a rectangular intensity profile. We oriented the lateral axis of the checkerboard so that the first orders appear at  $45^\circ$  and therefore are separated maximally from the transmitted beam on the detector. In addition, we added a strip of  $50\ \mu\text{m}$  of copper on the detector face to attenuate the transmitted pulse to the same intensity level as the first orders, so that it can be recorded with the first-order pulses without saturating the camera. In this way, in the same shot, an intensity profile of the original beam can be retrieved from the transmitted pulse with a high resolution, while the first-order diffractions provide the phase information. In case the transmitted beam is not recorded (e.g., it is used for an experiment after passing through a hole in the scintillator of the camera), the intensity information can be derived after the Fourier treatment of the shearograms, albeit only at the same resolution as the phase.

The fringes of the top-right and bottom-right first-order diffractions in Fig. 2 are analyzed using standard Fourier transform methods introduced by Takeda *et al.* [18] to retrieve the differential phase in two orthogonal directions. Due to the high-quality, low noise data, phase unwrapping can be done using the one-dimensional phase unwrapping routines available in most computer languages, in both the vertical and horizontal direction, taking the center of the image as the starting point. To invert the shear operator, the two orthogonal differential phase maps are combined to retrieve the phase of the beam itself, using the optimization algorithm described in Supplement 1. All algorithms were implemented in Python. The calculated wavefront of the actual X-ray beam at the camera position is shown in Fig. 3(a).

We then tested the result in the following way. We calculated the differential phase of the reconstructed wavefront of the beam,

in the same orthogonal directions as in the experimental data in Fig. 2. These calculated differential phases were compared with the actual measured differential phases, and we call their difference the residual differential phase error. This residual differential phase error is shown in Fig. 3(b) for the top-right interferogram, and in Fig. 3(c) for the bottom-right interferogram. The residual differential phase error is a measure of how well the reconstruction algorithm can find a wavefront that matches the measured data, and it is therefore a good indication of the overall (minimal) error of the whole phase retrieval procedure. The RMS value of the residual differential phase error over the beam aperture is  $\lambda/70$  for both Figs. 3(b) and 3(c).

With the wavefront and the intensity profile known to achieve great accuracy, the beam can be back propagated to the focal plane using a standard Fresnel propagator. The results, showing a beam focus with a full width at half maximum of  $79\ \text{nm}$  by  $113\ \text{nm}$  with the peak intensity of  $2.6 \times 10^{20}\ \text{W}/\text{cm}^2$ , are presented in Fig. 4.

#### 4. DISCUSSION AND CONCLUSION

To the best of our knowledge, we have presented a new method that uses two checkerboard diffraction gratings to perform shearing interferometry and reconstructed the full wavefront of a focused hard X-ray FEL pulse. From a single shot, the method allows for wavefront retrieval (to the resolution of a fraction of the X-ray wavelength) using the first-order diffraction pulses, as well as the intensity profile of the beam using transmitted pulse. The method compares favorably with many of the methods that have been used to determine the wavefront at XFEL and Synchrotron facilities in the last decade, such as scanning coherent diffraction microscopy or ptychography [6], Ronchi shearing interferometry [7,8], speckle tracking [26], and Talbot interferometry [9–13]. In ptychography, a nanostructured target is scanned through (or raster scanned close to the focus) in nanometer steps, and the resulting diffraction patterns are recorded and used in a phase-reconstruction algorithm. It is a very powerful microscopic technique that allows for the reconstruction of the sample, which is generally the main goal of X-ray microscopy and imaging beam-lines. However, purely from the focus determination point of view, it has several disadvantages in particular for XFELs. For example, for sub  $\mu\text{m}$  foci, high-resolution stages with nanometer precision are required, as well as a beam pointing stability of the similar order. Furthermore, multiple shots are needed for the reconstruction, and therefore shot-to-shot changes in the wavefront cannot be detected and will result in calculation errors. Similarly, the previously reported Ronchi shearing interferometry [7] is also not a single-shot technique, but it requires averaging over numbers of shots for wavefront reconstruction and would not allow the intensity profile retrieval at the same time.

In speckle tracking [26], the propagation in space of the speckles introduced by a scattering object is recorded, using two cameras that are placed at different distances from the scattering object. The camera placed closest to the target generally consist of a thin scintillator, so that a significant portion of the beam is transmitted and detected by the second camera. When it comes to wavefront reconstruction, the method can be very accurate (i.e.,  $100\ \text{mrad}$ ), with a spatial resolution limited to the speckle size at each detector. However the intensity profile of the original beam is not recorded. Furthermore, the detection requires two cameras separated by a meter or more, each of them mounted on its own X-ray microscope

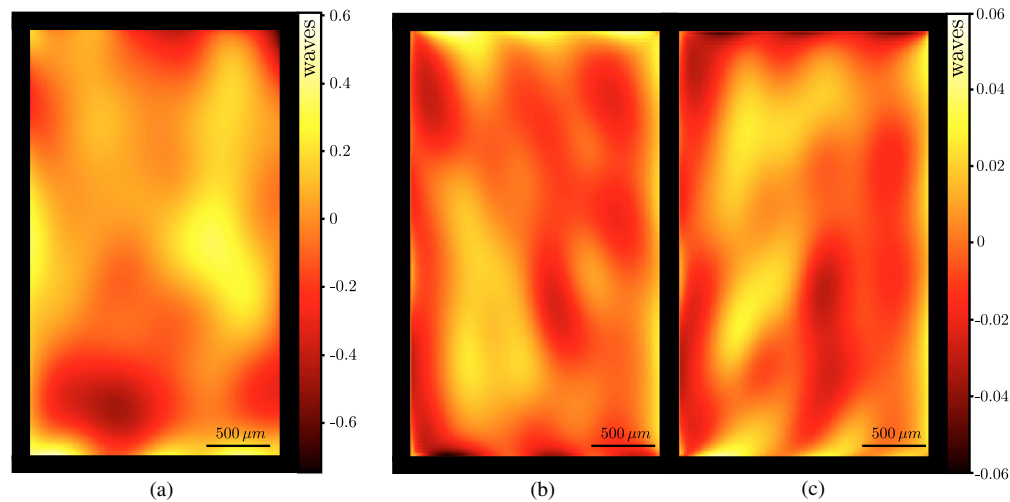


**Fig. 3.** (a) Reconstructed wavefront of the X-ray beam at the camera position, using two orthogonal differential phase measurements (i.e., top-right and bottom-right interference patterns in Fig. 2, and the algorithm described in Supplement 1. The X-ray beam has an RMS wavefront aberration of 0.16 waves. The residual differential phase errors (b and c), corresponding to the top-right and bottom-right shearograms in Fig. 2, respectively. The RMS of the residual differential phase error over the full-beam aperture is  $\lambda/70$  for both (b and c).

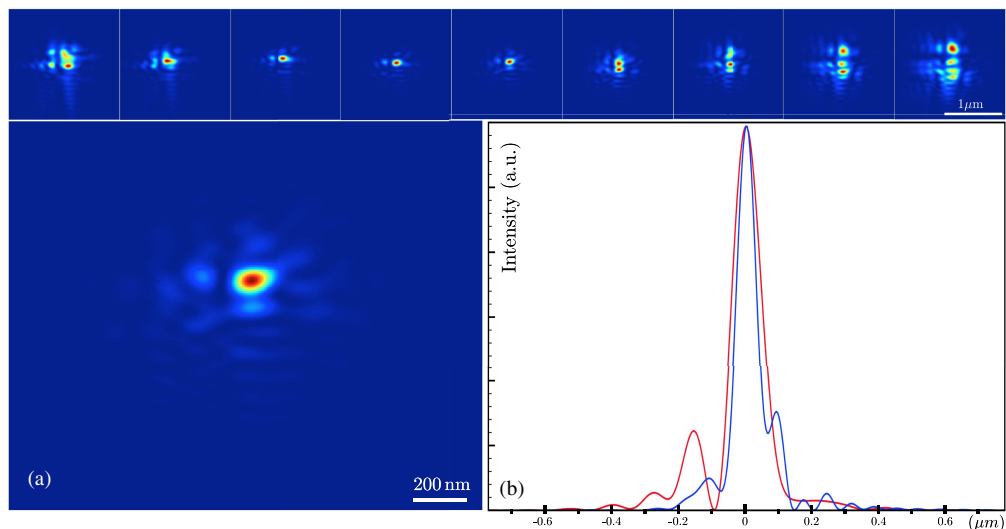


**Fig. 4.** Top: propagation of the X-ray beam around the focus. There is a 100  $\mu\text{m}$  distance in  $z$  between the images. (a) Image of the X-ray beam at the best focus and (b) line-out in the vertical (blue) and horizontal (red) direction, showing a full width at half maximum of 79 and 113 nm, respectively. With typical LCLS operation performance of 3 mJ and 50 fs, the peak intensity would be  $2.6 \times 10^{20} \text{ W/cm}^2$ .

imaging system; thus, the setup can become space demanding compared to Talbot or DGSI.

Another method, which has in the last few years become a standard at FEL facilities, uses Talbot interferometry: a two-dimensional-patterned transmission grating is placed in the beam, and a camera records the diffraction at the Talbot distance where the grating self-image reappears. Modulations in this image are used to retrieve the wavefront aberrations. The method has reported highly accurate wavefront measurements [10] (i.e., up to  $\lambda/100$ ), and it uses a fairly easy setup, with a single grating and a camera. For the optics used, Talbot gratings typically have pitches in the order of microns and larger, which are relatively easy to fabricate. On the contrary, the grating pitch for DGSI needs to be much smaller (i.e., order of 100 nm in our experiment) since the diffraction orders need to separate from the straight-through beam, and it requires even smaller pitches as the X-ray wavelength

becomes shorter. This particular point may become burdensome in a situation where very small spot sizes at high (e.g.,  $> 16 \text{ keV}$ ) photon energies need to be characterized. On the other hand, considering the setup and alignment constraints, Talbot method requires the grating-to-detector distance to be exactly at the Talbot distance. Thus, motorized positioning for a sufficient length along the optical axis, either for the grating or for the detector, is a prerequisite. Since this Talbot distance is photon-energy dependent, changes to the setup and interruption of experiment may be necessary when the photon energy of the beam is changed. This is usually not the case for the DGSI method described in this paper, where physical limitations are only mainly realized when the grating pitch is no longer sufficient to separate the transmitted beam from the diffracted beams.

In terms of the resolution and wavefront sensitivity, both Talbot and DGSI are shearing interferometry techniques, and thus, it is

well known that the precisions by these processes are highly dependent on the degree and contrast of the shear fringes [27]. Indeed, for DGS, when the shear approaches zero, the interferograms start to consist of nearly perfect linear fringes, even though the underlying beam may contain large aberrations. The more shear applied, the stronger the distortion of the fringes: the distortion in the interferograms due to second-order wavefront aberration scales linearly with the amount of shear, that of third-order aberrations scales quadratically with the amount of shear, etc. Therefore, larger shear values are desirable to achieve the highest sensitivity to the wavefront modulations. In DGS, this can be changed and optimized *in-situ* by changing the relative angle  $\alpha$  of the two gratings, or by changing the distance  $\ell$  between the gratings. In contrast, in the Talbot method, the shear is fixed by the grating pitch and relative distances of the grating and detectors to the focus, as mentioned above. Therefore, fine-tuning of such shear values may or may not be physically realizable in different experiment configurations. One must note that increasing the shear (i.e., increasing the angle  $\alpha$ ) will also increase the fringe frequency of the carrier (on the camera), as can be seen from Eq. (1), and obviously the fringes still need to be resolvable by the camera system. The DGS method in this manuscript allows one to tune the amount of shear (i.e., tune  $\alpha$ ) to achieve an ideal compromise between these two constraints for every particular setup. At the same time, the DGS method allows for a simultaneous measurement of the beam intensity profile with a resolution only limited by the detector pixel size, a versatility that none of the other methods has. Alternatively, if the direct beam is not captured on the camera (e.g., by using a scintillator with a hole), it can be used in a subsequent experiment with fully characterized wavefront on every shot with accuracy down to a fraction of the wavelength.

**Funding.** Office of Science (DE-AC02-76SF00515).

**Acknowledgment.** H. J. L., E. G., and B. N. are supported by the U.S. Department of Energy, Office of Science, Office of Fusion Energy Sciences under contract No. DE-AC02-76SF00515. Use of the Linac Coherent Light Source (LCLS), SLAC National Accelerator Laboratory, is supported by the U.S. Department of Energy, Office of Science, Office of Basic Energy Sciences under Contract No. DE-AC02-76SF00515.

**Disclosures.** The authors declare no conflicts of interest.

See [Supplement 1](#) for supporting content.

## REFERENCES

- M. Fuchs, M. Trigo, J. Chen, S. Ghimire, S. Schwartz, M. Kozina, M. Jiang, T. Henighan, C. Bray, G. Ndabashimiye, P. H. Bucksbaum, Y. Feng, S. Herrmann, G. A. Carini, J. P. Nad Philip Hart, C. Kenney, S. Guillet, S. Boutet, G. J. Williams, M. Messerschmidt, M. M. Seibert, S. Moeller, J. B. Hastings, and D. A. Reis, "Anomalous nonlinear x-ray Compton scattering," *Nat. Phys.* **11**, 964–971 (2015).
- K. Tamasaku, E. Shigemasa, Y. Inubushi, T. Katayama, K. Sawada, H. Yumoto, H. Ohashi, H. Mimura, M. Yabashi, K. Yamauchi, and T. Ishikawa, "X-ray two-photon absorption competing against single and sequential multiphoton processes," *Nat. Photonics* **8**, 313–316 (2014).
- K. Nass, L. Foucar, T. R. M. Barends, E. Hartmann, S. Botha, R. L. Shoeman, R. B. Doak, R. Alonso-Mori, A. Aquila, S. Sa Bajt, A. Barty, R. Bean, K. R. Beyerlein, M. Bublitz, N. Drachmann, J. Gregersen, H. O. Jonsson, W. Kabsch, S. Kassemeyer, J. E. Koglin, M. Krumrey, D. Mattle, M. Messerschmidt, P. Nissen, L. Reinhard, O. Sitsel, D. Sokaras, G. J. Williams, S. Hau-Riege, N. Timneanu, C. Caleman, H. N. Chapman, S. Boutet, and I. Schlichting, "Indications of radiation damage in ferredoxin microcrystals using high-intensity X-FEL beams," *J. Synchrotron Rad.* **22**, 225–238 (2015).
- S. M. Vinko, O. Ciricosta, B. I. Cho, K. Engelhorn, H.-K. Chung, C. R. D. Brown, T. Burian, J. Chalupsky, R. W. Falcone, C. Graves, V. Hajkova, A. Higginbotham, L. Juha, J. Krzywinski, H. J. Lee, M. Messerschmidt, C. D. Murphy, Y. Ping, A. Scherz, W. Schlotter, S. Toleikis, J. J. Turner, L. Vysin, T. Wang, B. Wu, U. Zastra, D. Zhu, R. W. Lee, P. A. Heimann, B. Nagler, and J. S. Wark, "Creation and diagnosis of a solid-density plasma with an x-ray free-electron laser," *Nature* **482**, 59–62 (2012).
- J. Chalupský, P. Boháček, T. Burian, V. Hájková, S. P. Hau-Riege, P. A. Heimann, L. Juha, M. Messerschmidt, S. P. Moeller, B. Nagler, M. Rowen, W. F. Schlotter, M. L. Swiggers, J. J. Turner, and J. Krzywinski, "Imprinting a focused x-ray laser beam to measure its full spatial characteristics," *Phys. Rev. Appl.* **4**, 014004 (2015).
- A. Schropp, R. Hoppe, V. Meier, J. Patommel, F. Seiboth, H. J. Lee, B. Nagler, E. C. Galtier, B. Arnold, U. Zastra, J. B. Hastings, D. Nilsson, F. Uhlén, U. Vogt, H. M. Hertz, and C. G. Schroer, "Full spatial characterization of a nanofocused x-ray free-electron laser beam by ptychographic imaging," *Sci. Rep.* **3**, 1633 (2013).
- B. Nagler, A. Aquila, S. Boutet, E. C. Galtier, A. Hashim, M. S. Hunter, M. Liang, A. E. Sakdinawat, C. G. Schroer, A. Schropp, M. H. Seaberg, F. Seiboth, T. van Driel, Z. Xing, Y. Liu, and H. J. Lee, "Focal spot and wavefront sensing of an x-ray free electron laser using Ronchi shearing interferometry," *Sci. Rep.* **7**, 13698 (2017).
- D. Nilsson, F. Uhlén, A. Holmberg, H. M. Hertz, A. Schropp, J. Patommel, R. Hoppe, F. Seiboth, V. Meier, C. G. Schroer, E. Galtier, B. Nagler, H. J. Lee, and U. Vogt, "Ronchi test for characterization of nanofocusing optics at a hard x-ray free-electron laser," *Opt. Lett.* **37**, 5046–5048 (2012).
- Y. Liu, M. Seaberg, D. Zhu, J. Krzywinski, F. Seiboth, C. Hardin, D. Cocco, A. Aquila, B. Nagler, H. J. Lee, S. Boutet, Y. Feng, Y. Ding, G. Marcus, and A. Sakdinawat, "High-accuracy wavefront sensing for x-ray free electron lasers," *Optica* **5**, 967–975 (2018).
- M. Seaberg, R. Cojocar, S. Berujon, E. Ziegler, A. Jaggi, J. Krempasky, F. Seiboth, A. Aquila, Y. Liu, A. Sakdinawat, H. J. Lee, U. Flechsig, L. Patthey, F. Koch, G. Seniutinas, C. David, D. Zhu, L. Mikeš, M. Makita, and P. Vagovic, "Wavefront sensing at x-ray free-electron lasers wavefront sensing at x-ray free-electron lasers," *J. Synchrotron Radiat.* **26**, 1115–1126 (2019).
- T. Inoue, S. Matsuyama, S. Kawai, H. Yumoto, Y. Inubushi, T. Osaka, I. Inoue, T. Koyama, K. Tono, H. Ohashi, M. Yabashi, T. Ishikawa, and K. Yamauchi, "Systematic-error-free wavefront measurement using an x-ray single-grating interferometer," *Rev. Sci. Instrum.* **89**, 043106 (2018).
- S. Rutishauser, L. Samoylova, J. Krzywinski, O. Bunk, J. Grünert, H. Sinn, M. Cammarata, D. M. Fritz, and C. David, "Exploring the wavefront of hard X-ray free-electron laser radiation," *Nat. Commun.* **3**, 947 (2012).
- S. Matsuyama, T. Inoue, J. Yamada, J. Kim, H. Yumoto, Y. Inubushi, T. Osaka, I. Inoue, T. Koyama, K. Tono, H. Ohashi, M. Yabashi, T. Ishikawa, and K. Yamauchi, "Nanofocusing of X-ray free-electron laser using wavefront-corrected multilayer focusing mirrors," *Sci. Rep.* **8**, 17440 (2018).
- S. Boutet and G. J. Williams, "The coherent x-ray imaging (cxi) instrument at the Linac Coherent Light Source (LCLS)," *New J. Phys.* **12**, 035024 (2010).
- M. Liang, G. J. Williams, M. Messerschmidt, M. M. Seibert, P. A. Montanez, M. Hayes, D. Milathianaki, A. Aquila, M. S. Hunter, J. E. Koglin, D. W. Schafer, S. Guillet, A. Busse, R. Bergan, W. Olson, K. Fox, N. Stewart, R. Curtis, A. A. Miahnahri, and S. Boutet, "The coherent x-ray imaging instrument at the Linac coherent light source," *J. Synchrotron Radiat.* **22**, 514–519 (2015).
- J. C. Wyant, "Double frequency grating lateral shear interferometer," *Appl. Opt.* **12**, 2057–2060 (1973).
- H. Schreiber and J. Schwider, "Lateral shearing interferometer based on two Ronchi phase gratings in series," *Appl. Opt.* **36**, 5321–5324 (1997).
- M. Takeda, H. Ina, and S. Kobayashi, "Fourier-transform method of fringe-pattern analysis for computer-based topography and interferometry," *J. Opt. Soc. Am.* **72**, 156–160 (1982).
- C. Elster, "Exact two-dimensional wave-front reconstruction from lateral shearing interferograms with large shears," *Appl. Opt.* **39**, 5353–5359 (2000).

20. C. Elster and I. Weingärtner, "Solution to the shearing problem," *Appl. Opt.* **38**, 5024–5031 (1999).
21. C. Elster, "Recovering wavefronts from difference measurements in lateral shearing interferometry," *J. Comput. Appl. Math.* **110**, 177–180 (1999).
22. C. Elster and I. Weingärtner, "Exact wave-front reconstruction from two lateral shearing interferograms," *J. Opt. Soc. Am. A*: **16**, 2281–2285 (1999).
23. P. Liang, J. Ding, Z. Jin, C.-S. Guo, and H. Tian Wang, "Two-dimensional wave-front reconstruction from lateral shearing interferograms," *Opt. Express* **14**, 625–634 (2006).
24. F. Siewert, J. Buchheim, S. Boutet, G. J. Williams, P. A. Montanez, J. Krzywinski, and R. Signorato, "Ultra-precise characterization of LCLS hard x-ray focusing mirrors by high resolution slope measuring deflectometry," *Opt. Express* **20**, 4525–4536 (2012).
25. M. Makita, P. Karvinen, V. Guzenko, N. Kujala, P. Vagovic, and C. David, "Fabrication of diamond diffraction gratings for experiments with intense hard x-rays," *Microelectron. Eng.* **176**, 75–78 (2017).
26. S. Berujon, E. Ziegler, and P. Cloetens, "X-ray pulse wavefront metrology using speckle tracking," *J. Synchrotron Radiat.* **22**, 886–894 (2015).
27. M. Servin, D. Malacara, and J. L. Marroquin, "Wave-front recovery from two orthogonal sheared interferometers," *Appl. Opt.* **35**, 4343–4348 (1996).